Ferroelectric vs. structural properties of large-distance sputtered epitaxial LSMO/PZT heterostructures

Philipp M. Leufke,[1] Robert Kruk,[1] Di Wang,[1,2] Christian Kübel,[1,2] and Horst Hahn[1,3]
[1]*Institute of Nanotechnology (INT), Karlsruhe Institute of Technology (KIT), Karlsruhe, Germany*
[2]*Karlsruhe Nano Micro Facility (KNMF), Karlsruhe Institute of Technology (KIT), Karlsruhe, Germany*
[3]*KIT-TUD-Joint Research Laboratory Nanomaterials/Technische Universität Darmstadt, Germany*

(Received 20 July 2012; accepted 17 September 2012; published online 25 September 2012)

We report on large-distance rf-magnetron sputtering as a competitive alternative to pulsed laser deposition and off-axis sputtering for the growth of epitaxial $PbZr_{0.52}Ti_{0.48}O_3$ (PZT) thin films. To determine the characteristics of the PZT films, the studies were focused on the interplay between microstructural and ferroelectric properties. The films were deposited on insulating or conducting (Nb-doped) $SrTiO_3$ and MgO substrates with $La_{0.83}Sr_{0.17}MnO_3$ as bottom electrode. The uniformity and homogeneity of the samples was demonstrated by using large area (1.0 mm^2) top electrodes. It is shown that epitaxial heterostructures of excellent crystalline and ferroelectric quality can be deposited from a stoichiometric PZT target without the need for excess PbO in the target or post-annealing of the samples. *Copyright 2012 Author(s). This article is distributed under a Creative Commons Attribution 3.0 Unported License*. [http://dx.doi.org/10.1063/1.4756997]

I. INTRODUCTION

Despite the ongoing quest for lead-free electronics, $Pb(Zr,Ti)O_3$ (PZT) thin films still play a major role in scientific research on memory applications and field-effect devices. In those and many other fields, the high switchable polarization and dielectric constant, long retention time with relatively low leakage and extensive tailorability of the ferro- and piezoelectric properties render PZT an unrivaled material of choice for pushing the technology limits.

One of the central problems common to all ferroelectrics is the gradual degradation of ferroelectric characteristics. In PZT thin films this is known to be caused by metal electrodes, so consequently conductive oxide electrodes were successfully used lowering leakage and fatigue effects. Along with conductive and superconductive oxides like IrO_2, RuO_2, ZnO and $YBa_2Cu_3O_{7-x}$[1–4] as electrode materials, conductive perovskites like $LaNiO_3$, $SrRuO_3$, $(La,Sr)CoO_3$, $Sr(Ti,Sb)O_3$ (SSTO), $(La,Sr)SnO_3$ (LSSO) and $(La,Sr)MnO_3$ (LSMO) have been in the focus of research, since they allow for heteroepitaxial growth with the PZT.[5–9]

Yet in the course of time it became apparent that the good match of the lattice constants between the electrode and PZT is not the only decisive characteristic determining the usefulness of a particular conducting oxide as an electrode;[10] what also matters is the type of the majority charge carriers in the electrode. Chen *et al.*[8] found that *n*-type perovskites (LSSO, SSTO) cause the ferroelectric hysteresis loops to broaden and the fatigue lifetime to be reduced dramatically. This behavior was attributed to the very nature of the PZT itself; presently PZT is considered to be a ferroelectric with all the characteristics of a wide bandgap *p*-type semiconductor.[11] When *n*-type electrodes are used, during the polarization cycling, accumulation of surface charge at the PZT/oxide interface (Schottky barrier) is observed. This brings about carrier injection which leads to accumulation of oxygen vacancies at the interface and in turn speeds up fatigue processes. The obvious way to overcome

 © Author(s) 2012

All article content, except where otherwise noted, is licensed under a Creative Commons Attribution 3.0 Unported license. See: http://creativecommons.org/licenses/by/3.0/
Downloaded to IP: 129.13.72.198 On: Tue, 29 Apr 2014 13:56:31

these problems, or at least to minimize them, was to choose a *p*-type conducting oxide, such as LSMO, as an electrode.[8]

However, choosing LSMO opens more research pathways to explore than just the optimization of ferroelectric properties of epitaxial LSMO/PZT heterostructures. This stems from the fact that LSMO is not merely a *p*-type conductor, but it is also a ferromagnet with magnetism primarily controlled by the carrier concentration. Indeed, in recent years there has been growing interest in multiferroic composites, where either magnetostrictive coupling between the piezoelectric PZT and LSMO is utilized[12] or where the high polarizability of the PZT is employed in field effect device structures for tuning the charge carrier density of the LSMO thin film.[12–17] The tuning of magnetic properties via applied voltage is in principle a surface (interface) effect due to the high concentration of the LSMO charge carriers, which limits the penetration depth of the electrostatic field. Consequently, smooth and clean LSMO/PZT interfaces with high crystallinity are necessary prerequisites for any appreciable magnetoelectric coupling.[16,17]

Basically, two classes of deposition techniques of oxide ferroelectrics have been established; one class comprises (metal-organic) chemical vapor deposition techniques and wet-chemical routes while the other one encompasses physical vapor deposition (PVD) methods like pulsed laser deposition (PLD), sputtering and oxide- or reactive-molecular beam epitaxy (MBE).

While each of the PVD methods can achieve very high quality films, they differ strongly regarding process requirements and their areas of applications. MBE ensures the highest accuracy of the elemental composition but requires reactive oxygen sources like ozone or plasma and a comprehensive control over a large number of process parameters.[18] For this reason, PLD and sputtering are much more widespread methods. The first is characterized by a generally good stoichiometry preservation and comparatively high deposition rates. On the downside, PLD requires costly and hazardous (excimer) laser equipment and is only suitable for homogeneous coating of comparatively small substrates; in some cases particle ejection from the target can occur,[9] destroying the film's crystallinity and raising the need for post-annealing.

Sputtering allows for homogeneous deposition on large substrates, but the elemental dependence of the sputtering yield at the target results in a generally limited control of the film stoichiometry.

In the case of PZT, a common requirement for all the PVD-based deposition processes is that the substrates need to be heated to temperatures of ≈525–700 °C during or after deposition in order to achieve epitaxial growth of the perovskite phase.[19] Due to the high vapor pressure of PbO,[20] an excess of PbO in the vapor phase above the sample surface is necessary, leading to a self-stabilized stoichiometry above a critical temperature in an interval of ≈550–650 °C.[19,21] As a consequence, as-grown films possess correct Pb stoichiometry but are prone to Pb loss during post-annealing; thus, rapid thermal annealing is often employed as a compromise between improved crystallinity and degraded stoichiometry.[19,22]

Although PZT can be reactively sputtered from metallic targets in direct current (dc) mode,[23,24] radio frequency (rf) magnetron sputtering from readily sintered compound targets is the most established method, often employing targets with 10–20 mol% excess PbO.[18,22] However, when epitaxial growth without post-annealing is to be achieved, the tuning of the deposition parameters – namely substrate temperature, O_2 and Ar partial pressures, target-substrate separation, sputtering power and dc-bias voltage – can be a daunting task. Another challenge, again raising the need for post-annealing, is the degradation of crystallinity of oxide thin films as a result of the bombardment with high energetic oxygen ions repelled from the target. As a workaround, off-axis sputtering is employed, which avoids the oxygen bombardment, but also significantly reduces the deposition rate and film homogeneity on large wafers and does not allow for simultaneous or sequential multi-target operation.

Our approach to tackle these issues is to drastically increase the target-substrate separation d_{sep} while simultaneously adjusting the working pressure to reduce the mean free path of the oxygen ions well below d_{sep} causing all species to be thermalized before reaching the substrate.[23,25–27] This concept was recently successfully demonstrated for the deposition of high quality epitaxial LSMO thin films.[28]

The on-axis geometry allows for accommodation of many sources, to do co-deposition and/or switching between the sources within very short time, resulting in clean interfaces in multilayer

All article content, except where otherwise noted, is licensed under a Creative Commons Attribution 3.0 Unported license. See: http://creativecommons.org/licenses/by/3.0/
Downloaded to IP: 129.13.72.198 On: Tue, 29 Apr 2014 13:56:31

systems. Additionally, the large distance ensures uniform vapor diffusion and thus enables a more homogeneous film deposition even on larger substrates. Thus, 285 mm was chosen as opposed to the typical distances in sputtering systems of around 30–100 mm. As a positive side effect, stoichiometric PZT targets can be used, since the Pb/(Zr+Ti) ratio is known to rise with increasing distance,[22] which can be explained by the reduced scattering angle of heavier species during the thermalization process.[29]

In the following it will be shown that large-distance magnetron sputtering is a promising alternative to other well-established PVD methods in terms of crystalline and functional characteristics of the heterostructures. After the presentation of the experimental procedures, the high quality of the LSMO/PZT bilayers prepared by the large-distance sputtering method, regarding interface smoothness, stoichiometry, crystallinity and ferroelectric properties will be demonstrated.

II. EXPERIMENTAL DETAILS

The deposition of the LSMO and PZT thin films was carried out in a custom-built sputtering chamber (Createc Fischer GmbH). The chamber comprises eight 3″ magnetrons in an octagonal geometry, where the substrate is located in the center in an on-axis geometry with an angle of incidence (with respect to the substrate's surface normal) of 37.5 ° and a target-substrate distance of 285 mm. Up to four different substrates can be mounted on the halogen-lamp heated manipulator and rotated at a speed of ≈7 rpm, to ensure a homogeneous distribution of heat and deposited material.

Stoichiometric $La_{0.65}Sr_{0.35}MnO_3$ (elastomer-bonded) and $PbZr_{0.52}Ti_{0.48}O_3$ (In-Sn bonded) targets were provided by Kurt J. Lesker and SurfaceNet company. The latter also supplied the (100) oriented epi-polished single-crystal $SrTiO_3$ (STO), $SrTiO_3$:Nb(0.5 wt.%) (STO:Nb) and MgO substrates.

To evaporate adsorbates, the as-purchased substrates were heated to 850 °C for more than one hour in ultra-high vacuum (UHV). Then 5–7 nm thin LSMO layers were rf-sputtered at a working pressure of 0.018 mbar in an $O_2/(Ar+O_2)$ ratio of 40 % and a substrate temperature of 800 °C – as described in Ref. 28 – resulting in a stoichiometry of $La_{0.83}Sr_{0.17}MnO_3$, as determined by Rutherford backscattering spectroscopy, confirming a loss of ≈50 % of Sr.[28] This loss can again be explained by the larger scattering angles of the lighter (Sr) as compared to the heavier species (La).[22,29]

For the PZT deposition, the samples were heated to 550 °C. The PZT films of 90 nm thickness were rf-sputtered in 20 % O_2 at a working pressure of 0.003 mbar, yielding a growth rate of 3 Å/min. The rf power density for the PZT deposition was kept constant at 4.4 W/cm^2. After the PZT deposition, the samples were cooled down in 0.007 mbar pure oxygen.

All temperature ramps were performed at a rate of 6 K/min and the samples were kept in UHV between all steps. For comparison, samples without the LSMO back electrode were produced using identical conditions.

In a last step, square-shaped Au contacts with an area of 1.0 mm^2 and a thickness of 25 nm were dc-sputtered through a shadow mask. Gold was chosen as top electrode material, as it is known to cause lower leakage than Pt electrodes at electric fields below 400 kV/cm.[30]

The samples were investigated using a variety of analytical methods to get insight into both microstructural and functional, i.e. ferroelectric (FE), properties. The film thickness was monitored during deposition by a quartz crystal microbalance (QCM), which was calibrated by X-ray reflectometry (XRR) for the respective materials. High-resolution X-ray diffraction (HRXRD) in θ-2θ geometry was used to determine the crystalline quality in growth direction accompanied by reciprocal space mapping (RSM) to examine the structural quality, lattice relaxation and the in-plane lattice components.

Additionally, scanning transmission electron microscopy (STEM) and selected area electron diffraction (SAED) were performed on focused ion beam (FIB) prepared cross-sections of representative samples in a FEI Titan 80-300 electron microscope operated at 300 kV, to study their crystal structure and the interface between the substrate and film. The local chemical composition was revealed by energy dispersive X-ray spectroscopy (EDX) on STEM cross-sections.

All article content, except where otherwise noted, is licensed under a Creative Commons Attribution 3.0 Unported license. See: http://creativecommons.org/licenses/by/3.0/
Downloaded to IP: 129.13.72.198 On: Tue, 29 Apr 2014 13:56:31

A Radiant RT66B tester was employed to measure the ferroelectric properties of the devices which were contacted with tungsten needles in a probe station with the tester's drive output connected to the bottom electrode, as recommended to reduce noise pickup.

III. RESULTS AND DISCUSSIONS

Additionally to monitoring the deposition rates by a calibrated QCM, XRR was performed on selected samples to verify the actual film thickness. With a growth rate of 3 Å/min, the large-distance sputtering method is about two times slower than off-axis sputtering[17] and up to ten times slower than PLD. However, if sputtering rate were of importance, it could still be increased by reaching the rf power density limit of the PZT target, and/or by co-deposition from two or more targets.

In order to evaluate the value of large-distance rf-sputtering in comparison with off-axis sputtered or PLD grown PZT thin films, extensive microstructural and functional ferroelectric studies were carried out.

A. Microstructural Characterization

The microstructure of all samples was characterized by means of HRXRD. The θ-2θ scans of LSMO/PZT heterostructures grown on STO and MgO in Fig. 1 show phase-pure growth of the perovskite PZT film along the ⟨001⟩ direction on top of the epitaxial LSMO layer of the same orientation.[28] The satellites of the LSMO (002) reflex, which form a shoulder at the STO (002) peak, are typical finite thickness oscillations. The same kind of so-called Laue fringes are also visible in the high-definition scan (Fig. 1(b)) which was recorded around the PZT (001) reflex. For 90 nm thick films, the occurrence of these oscillations is particularly rare – especially since the PZT does not grow commensurately (see below) –, as it requires highest film homogeneity and extremely smooth interfaces. Both, the thickness as calculated from the fringes spacing as well as the low interface roughness of less than 0.3 nm were confirmed by XRR (not shown).

Because of the high lattice mismatch, even very thin films of LSMO cannot be grown fully strained on MgO.[28] The in-plane relaxation of the LSMO causes the PZT layer on top to develop pronounced mosaicity, which can be seen in the rocking curves in Fig. 1(c). In comparison, the full width at half maximum (FWHM) values for PZT on STO/LSMO is much smaller and as low as the best values for PLD grown[8] and off-axis sputtered[17] $PbZr_xTi_{1-x}O_3$ films despite the fact that the present films are much thinner than those reported in literature (90 nm vs. 250 nm); it is known that FWHM usually increases with decreasing thickness in case of highly mismatched layers.[31] It is worth pointing out that Vaz *et al.* found that such high crystallinity could not be achieved with all-sputtered LSMO/PZT films on STO in off-axis geometry;[17] instead, their LSMO layer was deposited by MBE. In their case the sharpness of the rocking curves was likely an an extra benefit of using TiO_2-terminated STO substrates and the lower lattice mismatch of the employed $PbZr_{0.2}Ti_{0.8}O_3$.

PZT layers directly deposited onto the respective substrates, without the LSMO buffer layer, were crystallographically very similar in case of STO and STO:Nb substrates, while on MgO phase pure perovskite PZT growth could not be achieved. Apparently, the relaxed LSMO film, which provides a compressive misfit strain as opposed to the tensile misfit strain from the MgO, acts as a seed layer to the PZT film and helps to stabilize the perovskite phase. On STO there is no such effect since the LSMO layer grows commensurately, retaining the in-plane lattice constant of the substrate for further PZT layer growth.

In order to investigate the influence of the in-plane lattice misfit of the substrates, RSMs on the (204) reflexes were recorded for the same samples as shown in Fig. 1. On the STO/LSMO substrate, the in-plane lattice of the PZT layer relaxes coherently, reaching similar peak broadening like in perpendicular direction (Fig. 2(a)). With lattice constants of $a = 4.05$ Å and $c = 4.18$ Å, the in-plane component is very close to the bulk literature value[32] of $a_{\text{bulk}} = 4.036$ Å, while the c lattice constant is slightly bigger compared to $c_{\text{bulk}} = 4.146$ Å. The increased c lattice constant might be ascribed to a slight oxygen deficiency[9] which may be offset by post-deposition cool-down in a higher oxygen partial pressure of up to atmospheric pressure, which is a common practice.[8,9,17,33]

All article content, except where otherwise noted, is licensed under a Creative Commons Attribution 3.0 Unported license. See: http://creativecommons.org/licenses/by/3.0/
Downloaded to IP: 129.13.72.198 On: Tue, 29 Apr 2014 13:56:31

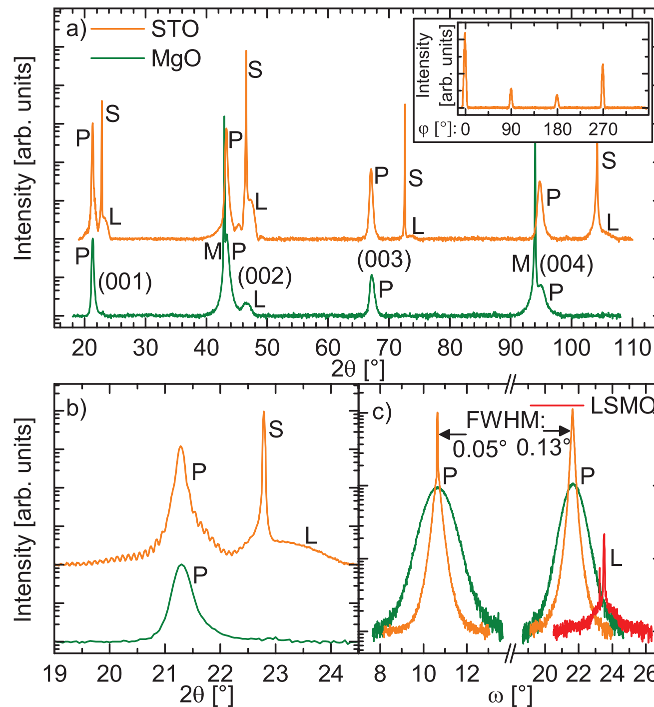

FIG. 1. HRXRD analysis of simultaneously deposited STO/LSMO(6.5 nm)/PZT(90 nm) and MgO/LSMO(6.5 nm)/PZT(80 nm) heterostructures; a): θ-2θ-scan, b): close-up view of the (001) region, illustrating the Laue oscillations of the STO sample, c): rocking curves on LSMO and PZT peaks at the first and second order. The inset in a) shows a φ-scan on the (204) reflection of the PZT layer on STO/LSMO. The annotations P, L, S and M in the plots indicate the affiliation of the reflections for PZT, LSMO, STO and MgO, respectively.

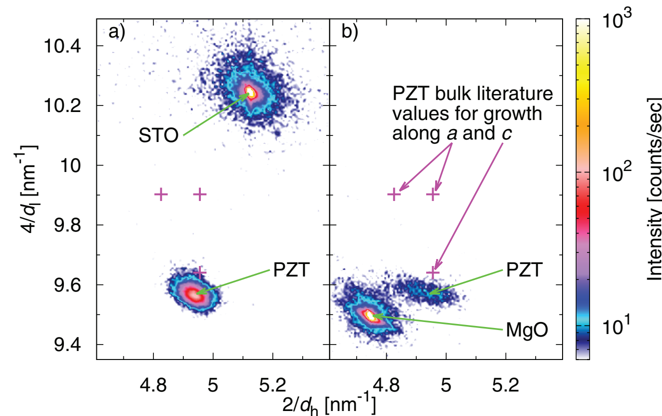

FIG. 2. RSMs on the asymmetric (204) reflection of simultaneously deposited LSMO/PZT heterostructures, with the corresponding unstrained locations for *a*- and *c*-oriented growth of PZT as indicated. a): STO/LSMO(6.5 nm)/PZT(90 nm) and b): MgO/LSMO(6.5 nm)/PZT(80 nm). Pure *c*-oriented growth with slightly increased lattice constants is apparent.

In contrast, while featuring the same *a* and *c* lattice constants like on STO/LSMO, the horizontal distribution (i.e. along the ω scan direction) of the PZT (204) diffraction of the film on MgO/LSMO is much broader (Fig. 2(b)), which is a consequence of the mosaicity observed in the rocking curves of the symmetric reflections (Fig. 1(c)), but may also be caused by a slightly broader distribution of the in-plane lattice constant.

As the LSMO layer is invisible in the RSMs due to its small thickness, STEM images were collected in order to investigate the strain relaxation at the LSMO and PZT interfaces. Despite

All article content, except where otherwise noted, is licensed under a Creative Commons Attribution 3.0 Unported license. See: http://creativecommons.org/licenses/by/3.0/
Downloaded to IP: 129.13.72.198 On: Tue, 29 Apr 2014 13:56:31

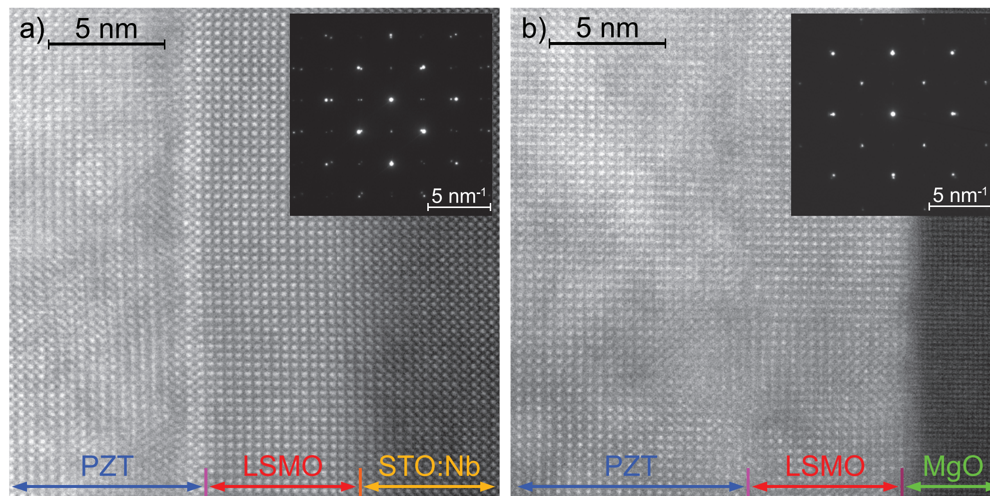

FIG. 3. STEM cross-sections of the interfacial region of simultaneously deposited a): STO:Nb/LSMO(6.5 nm)/PZT(90 nm) and b) MgO/LSMO(6.5 nm)/PZT(80 nm) heterostructures. The insets show SAED patterns recorded at an equivalent area with similar crystal orientations, covering substrate, LSMO and PZT.

the slight difference in the Sr doping level (17 % instead of 12 %), the LSMO layer still grows cube-on-cube on top of the STO:Nb substrate, confirming our previous results[28] (Fig. 3(a)). The LSMO/PZT bilayer features a very sharp interface, as could be expected from the Laue fringes observed in HRXRD (Fig. 1(b)). The high compressive misfit strain only allows the first two unit cells of PZT to grow commensurately over the whole investigated range, as evidenced in *Z*-contrast STEM image (Fig. 3(a)) by the higher intensities on Pb atomic columns compared to La columns. The massive strain relaxation was induced in form of extended dislocations and small highly distorted or even amorphous grains (not shown) located within a region of $\approx$5 nm at the interface. Beyond the relaxation region, the PZT film is single crystalline throughout the entire film thickness, as confirmed by SAED, which shows sharp diffractions for both layers, LSMO and PZT.

As expected, the LSMO/PZT bilayers deposited on STO and STO:Nb substrates were virtually identical in their microstructural properties.

On the MgO substrate, the tensile misfit strain forces the LSMO layer to immediately accommodate by means of tilting, bending and dislocations (Fig. 3(b)). The reduced coherence apparently affects the LSMO/PZT interface, blurring it noticeably. As a consequence, the disturbed interface region extends up to $\approx$10 nm until the PZT accommodates and forms a single-crystalline layer. Also from the RSM (Fig. 2(b)) it can be concluded, that the disorder induced by the strain relaxation of the LSMO layer has significant impact on the PZT crystallinity.

Another interesting fact is that the PZT film on MgO/LSMO only measures 80 nm in contrast to the 90 nm of the simultaneously deposited films on STO/LSMO and STO:Nb/LSMO although all the substrates were mounted at equivalent positions on the rotating sample holder. As the PZT lattice constants are identical for all three systems, this deviation can only be attributed to the different interface quality.

For elemental analysis, EDX was performed in the STEM mode, determining ratios of 56 $\pm$ 5 % and 54 $\pm$ 5 % for Zr/(Zr+Ti) and Pb/(Pb+Zr+Ti), respectively. As expected, the large target-substrate distance seems to compensate for the PbO loss which normally occurs due to the elevated substrate temperature.

B. Ferroelectric Properties

Following a common practice, the top electrodes were deposited through shadow masks. When sputtering or PLD are employed, the resulting actual dimensions of the top electrodes (TE) may

All article content, except where otherwise noted, is licensed under a Creative Commons Attribution 3.0 Unported license. See: http://creativecommons.org/licenses/by/3.0/
Downloaded to IP: 129.13.72.198 On: Tue, 29 Apr 2014 13:56:31

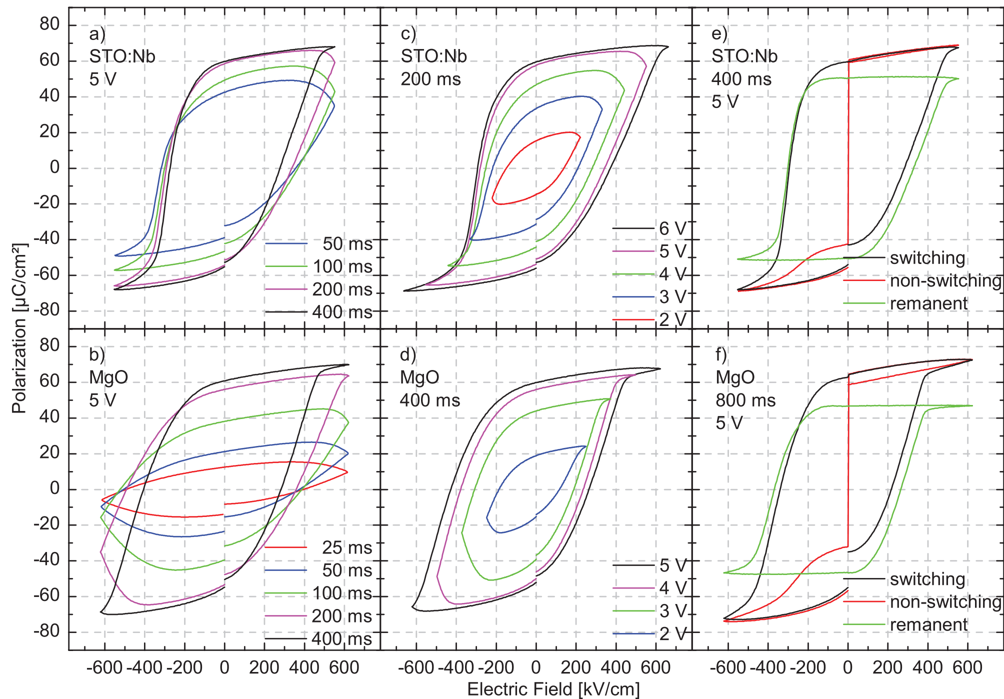

FIG. 4. FE properties of 1.0 mm^2 large STO:Nb/LSMO(5.0 nm)/PZT(90 nm)/Au (upper row) and MgO/LSMO(6.5 nm)/PZT(80 nm)/Au (lower row) capacitor structures, with cycle times and voltages as denoted in the graphs; a) & b): cycle time dependence; c) & d): voltage dependence; e) & f): remanent hysteresis.

vary substantially due to the diffuse material flow. The deviation from the nominal electrode area is affected by the working pressure, the distance between mask and sample and the lateral dimensions of the masks, with higher error for smaller structures. To assure reliable polarization values, accurate determination of the TE area was done with special care. Before proceeding to ferroelectric tests, all samples were analyzed in an optical microscope and the TE area was calculated using the ImageJ image processing software.

For the ferroelectric characteristics, the size of the TE is of importance since the likelihood of incorporating crystal defects and pinholes scales exponentially with the area. As a consequence, typical lateral dimensions, which are still comfortably accessible in a probe station, are of 50–100 μm; an electrode area of 0.05 mm^2 is already considered “large”.[17] Apart from having investigated FE devices as small as 0.025 mm^2, in order to demonstrate the lateral homogeneity of the LSMO/PZT heterostructures and their suitability for future magnetoelectric tuning, the focus of this report is on devices with a TE area of 1.0 mm^2, two orders of magnitude larger than common structure sizes.

The disadvantage of such large TEs is that the effective capacity of these ferroelectric capacitor devices is so high, that the resistance of the leads – especially of the LSMO bottom electrode (BE) – has significantly increased the circuit’s time constant $\tau = RC$. As a consequence, LSMO films thinner than 6.5 nm on MgO substrates due to their high resistance did not allow for the saturation of the PZT polarization. For the same reason conductive STO:Nb was preferred over insulating STO substrates for FE measurements; however, the resistance of the STO:Nb substrates is still in the 10 kΩ range. While devices as small as of 0.025 mm^2 exhibited saturating P vs. E hysteresis loops at cycle times of 10 ms (100 Hz) and below, the 1.0 mm^2 large devices proved to require much longer cycle times, as shown in Fig. 4(a) and 4(b).

Although the STO:Nb substrate has a lower resistance, enabling faster PZT charging, its combination with LSMO buffer layer brings about an asymmetry in the switching behavior with the right hand side requiring longer time or higher voltage (see Fig. 4(c)) to reach FE saturation. This can be explained by the p-n junction formed between the LSMO layer and the STO:Nb substrate, which is

All article content, except where otherwise noted, is licensed under a Creative Commons Attribution 3.0 Unported license. See: http://creativecommons.org/licenses/by/3.0/
Downloaded to IP: 129.13.72.198 On: Tue, 29 Apr 2014 13:56:31

in reverse bias when applying positive voltages at the STO:Nb, thus causing a voltage drop at the junction and reducing the charging current significantly.

Again, the effect of the electrode charge carrier type on the polarization switching could clearly be seen in PZT films grown directly on STO:Nb without the LSMO buffer layer. They showed very poor performance with low remanence, which is most likely attributed to the fact that STO:Nb as an *n*-type conductor is not a best choice as an electrode for *p*-type PZT thin films.[8]

Fig. 4(b) illustrates the difficulties in the switching at higher frequencies of PZT layer on MgO/LSMO, due to the high resistance of the LSMO BE. Only at relatively long cycle time of 400 ms, the square-like polarization loops indicate full charging with symmetric charging currents (unlike for the STO:Nb sample with the *p*-*n* junction). However, another effect, an imprint shift of ≈ -60 kV/cm, becomes apparent. This shift is also present in the STO:Nb samples, albeit disguised by the asymmetric charging currents. The imprint is also the cause for the asymmetry in the MgO samples' hysteresis loops, when the cycle time is too short (Fig. 4(b)) or the voltage too low (Fig. 4(d)) for full saturation at negative electric fields.

The observed imprint is well known in literature, especially in cases where the TE and BE materials differ,[34] with interpretations and explanations including misfit strain effects and/or oxygen loss at the LSMO/PZT interface,[10,35] electrons and/or Pb vacancies being trapped at the top interface,[36,37] charge compensation for oxygen vacancies generated at the TE interface[37,38] and defect-dipole complexes due to oxygen vacancies.[37,39,40]

A fundamental feature of the ferroelectric is the genuine remanent polarization P_r which can be extracted from the FE hysteresis loops by subtracting parasitic contributions, such as linear capacitances and leakage currents (Fig. 4(e) and 4(f)). This measurement mode applied is closely related to the standardized PUND (positive up, negative down) test,[41,42] but with triangular pulse shape, like in hysteresis measurements. The basic idea of this method rests on the fact that the purely capacitive dielectric charge contributions result in straight lines versus sweeping voltage, while leakage currents lead to open half-loops which can subsequently be subtracted exposing the actual remanent polarization charge.

In our heterostructures one can see right away that the leakage at positive electric fields is very low in both cases, even at these low cycle frequencies, while there is a significant contribution at negative electric fields. This obvious asymmetry can again be ascribed to the different bottom and top electrode materials. As Scott *et al.* reported,[43] there is an *n*-type oxygen deficient region in the PZT located at the metal electrode interface, creating an *n*-*m* Schottky junction between the PZT and the Au electrode.

Thus, at negative voltages applied to the BE, this Schottky junction is in forward bias, effectively allowing a leakage current, while blocking it when the voltage bias gets reversed.

While the physically meaningful P_r is determined from the remanent hysteresis loops, resulting in $\approx 50\ \mu C/cm^2$ for the present PZT thin films, it is sometimes difficult to make a straightforward comparison with the values reported in the literature since they are often based on the standard hysteresis loops, where the parasitic contributions are still present (here: $\approx 60\ \mu C/cm^2$). In any case, for the given PZT stoichiometry, the P_r of the large-distance sputtered PZT films is as high as any of the best, mostly PLD-grown, films reported in literature.[8,9,15]

Regarding the coercive electric field E_c, the values reported in the literature are usually 3–4 times lower. However, the common thicknesses of epitaxial PZT films are usually around 2.5–6 times larger[8,9,11,15] and E_c is known to increase with decreasing thickness,[44] especially when metallic top electrodes are employed.[21] Moreover, epitaxial films are known to have higher E_c compared to textured films.[21]

It is worth mentioning that the remarkably good FE properties of the large-distance sputtered PZT thin films are another indication of the correct Pb stoichiometry yielded by this deposition method.[18,45]

Two other figures of merit for ferroelectric devices are their retention and fatigue characteristics. The retention measurements are presented in Fig. 5(a). There is an apparent difference between the STO:Nb and the MgO samples. While the STO:Nb sample shows virtually no loss of remanent polarization, the MgO sample drops by ≈ 20 % within 3 days. The lower retention on MgO can be explained by the defective interface region between the distorted LSMO BE and the PZT, creating a

All article content, except where otherwise noted, is licensed under a Creative Commons Attribution 3.0 Unported license. See: http://creativecommons.org/licenses/by/3.0/
Downloaded to IP: 129.13.72.198 On: Tue, 29 Apr 2014 13:56:31

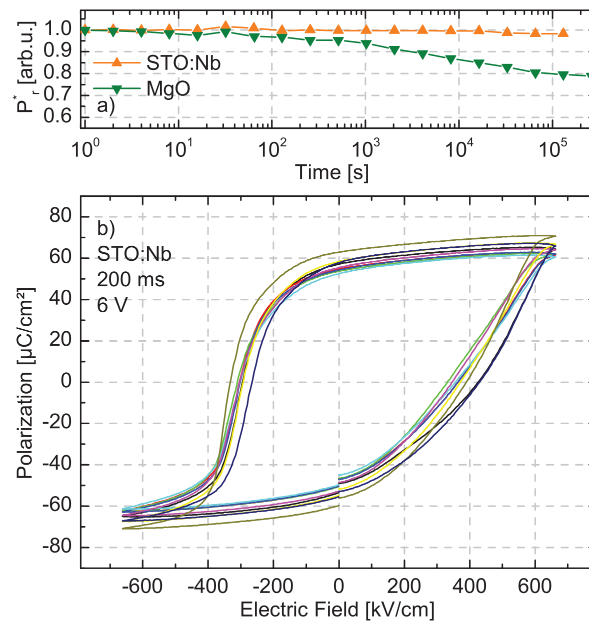

FIG. 5. a): Retention of 1.0 mm^2 LSMO/PZT/Au capacitors grown on STO:Nb and MgO. b): FE hysteresis curves of nine out of twelve 1.0 mm^2 LSMO/PZT/Au devices deposited on a single STO:Nb substrate.

ferroelectrically dead layer which in turn leads to the increased depolarization field inside the PZT layer. As a result in the course of time, the remanent polarization in MgO/LSMO/PZT gets reduced much faster than in STO:Nb/LSMO/PZT.

In this context, the high retention of the STO:Nb sample, being much better than for the rf-sputtered and post-annealed STO/LSMO/PZT systems reported by Ray *et al.*,[46] is again in accordance with our claim of the high interfacial quality indicated by the HRXRD Laue oscillations.

The fatigue testing was omitted because of the low frequencies required for reliable switching of the device in each cycle; furthermore, low fatigue is only expected for symmetric perovskite electrodes.[8,9]

Another criterion of the quality of deposition methods of FE thin films is yield of functioning devices per unit area, which is a measure of thin film uniformity and homogeneity. As stated above, this yield highly depends on the lateral size of the capacitor structure, as the probability for defects scales exponentially with the TE area. With the large-distance sputtering methods the average yields were higher than 50 % on MgO substrates and more than 75 % on STO:Nb; Fig. 5(b) illustrates the very similar FE hysteresis curves of nine out of twelve 1.0 mm^2 large devices grown on a single substrate. Assuming a binomial distribution for the defect probability, the corresponding yields for typical (100 μm)^2 devices reach up to >99.3 % and >99.7 % on MgO and STO:Nb, respectively. It should also be noted that this high device yield was achieved without any clean-room equipment and any substrate etching prior to deposition.

IV. SUMMARY

Phase-pure epitaxial PZT thin films with LSMO bottom electrodes were deposited on STO, STO:Nb and MgO substrates by means of large-distance rf magnetron sputtering from a stoichiometric PZT target without a need for excess PbO. The extraordinarily smooth PZT interfaces in the LSMO/PZT/Au heterostructures on STO and STO:Nb were evidenced through the presence of Laue oscillations in HRXRD patterns.

On MgO substrates the LSMO seed layer stabilized the perovskite phase, leading to *c*-axis oriented growth of the PZT layers; on STO and STO:Nb the LSMO layer had no influence on the microstructure thanks to the commensurate growth of the thin LSMO films. However, the

All article content, except where otherwise noted, is licensed under a Creative Commons Attribution 3.0 Unported license. See: http://creativecommons.org/licenses/by/3.0/
Downloaded to IP: 129.13.72.198 On: Tue, 29 Apr 2014 13:56:31

ferroelectric properties of PZT on STO:Nb got immensely improved by introducing the LSMO buffer layer, a fact that can be explained by the different charge carrier types; *p*-type conductivity of LSMO in contrast to the *n*-type STO:Nb.

Both 1.0 mm^2 large LSMO/PZT/Au capacitor structures grown on STO:Nb and on MgO, exhibited state-of-the-art ferroelectric properties with high remanent polarization and pronounced coercivity.

With respect to crystalline and ferroelectric quality of the PZT thin films, the large-distance sputtering technique proved to be a serious competitor to the best-adjusted PLD and off-axis sputtering methods described in the literature. Although at the expense of low deposition rate, it provides significant flexibility in fabrication procedures without compromising the quality of heterostructures. Main advantages include co- or sequential deposition of multilayers – without the need for post-annealing – and large-area uniformity typical of on-axis sputtering.

ACKNOWLEDGMENTS

This work was partially supported by the Deutsche Forschungsgemeinschaft (DFG) under contract HA1344/28-1. The authors acknowledge support from the KNMF laboratory for spectroscopy and microscopy and the State of Hessen.

[1] T. Nakamura, Y. Nakao, A. Kamisawa, and H. Takasu, Applied Physics Letters **65**, 1522 (1994).
[2] H. N. Al-Shareef, O. Auciello, and A. I. Kingon, Journal of Applied Physics **77**, 2146 (1995).
[3] X. Wang, Y. Wang, J. Yin, and Z. Liu, Scripta Materialia **46**, 783–787 (2002).
[4] R. Ramesh, W. K. Chan, B. Wilkens, H. Gilchrist, T. Sands, J. M. Tarascon, V. G. Keramidas, D. K. Fork, J. Lee, and A. Safari, Applied Physics Letters **61**, 1537 (1992).
[5] M.-S. Chen, T.-B. Wu, and J.-M. Wu, Applied Physics Letters **68**, 1430 (1996).
[6] C. B. Eom, R. B. Van Dover, J. M. Phillips, D. J. Werder, J. H. Marshall, C. H. Chen, R. J. Cava, R. M. Fleming, and D. K. Fork, Applied Physics Letters **63**, 2570 (1993).
[7] R. Ramesh, H. Gilchrist, T. Sands, V. G. Keramidas, R. Haakenaasen, and D. K. Fork, Applied Physics Letters **63**, 3592 (1993).
[8] F. Chen, Q. Z. Liu, H. F. Wang, F. H. Zhang, and W. Wu, Applied Physics Letters **90**, 192907 (2007).
[9] W. Wu, K. H. Wong, C. L. Choy, and Y. H. Zhang, Applied Physics Letters **77**, 3441 (2000).
[10] W. Wu, Y. Wang, G. K. H. Pang, K. H. Wong, and C. L. Choy, Applied Physics Letters **85**, 1583 (2004).
[11] O. Auciello (Ed.), *Science and technology of electroceramic thin films* (Kluwer Academic, Dordrecht, The Netherlands, 1995).
[12] I. Vrejoiu, M. Ziese, A. Setzer, P. D. Esquinazi, B. I. Birajdar, A. Lotnyk, M. Alexe, and D. Hesse, Applied Physics Letters **92**, 152506 (2008).
[13] X. Hong, A. Posadas, A. Lin, and C. Ahn, Physical Review B **68**, 1–5 (2003).
[14] C. Thiele, K. Dörr, W.-M. Lin, K.-H. Müller, and L. Schultz, Sensors and Actuators A **129**, 180–183 (2006).
[15] S. Dussan, A. Kumar, J. F. Scott, and R. S. Katiyar, Applied Physics Letters **96**, 9 (2010).
[16] C. A. F. Vaz, J. Hoffman, Y. Segal, J. W. Reiner, R. D. Grober, Z. Zhang, C. H. Ahn, and F. J. Walker, Physical Review Letters **104**, 3–6 (2010).
[17] C. A. F. Vaz, Y. Segal, J. Hoffman, F. J. Walker, and C. H. Ahn, J. Vac. Sci. Technol. B **28**, C5A6 (2010).
[18] N. Izyumskaya, Y. I. Alivov, S. J. Cho, H. Morkoç, H. Lee, and Y. S. Kang, Critical Reviews in Solid State and Materials Sciences **32**, 111–202 (2007).
[19] P. Muralt, Journal of micromechanics and microengineering **10**, 136–146 (2000).
[20] Y. Hwang, Journal of Materials Science Letters **14**, 9–10 (1995).
[21] J. F. M. Cillessen, M. W. J. Prins, and R. M. Wolf, Journal of Applied Physics **81**, 2777 (1997).
[22] G. Velu, D. Remiens, and B. Thierry, Journal of the European Ceramic Society **17**, 1749–1755 (1997).
[23] K. Sreenivas and M. Sayer, Journal of Applied Physics **64**, 1484 (1988).
[24] S. Kalpat and K. Uchino, Journal of Applied Physics **90**, 2703 (2001).
[25] T. Motohiro and Y. Taga, Thin Solid Films **112**, 161–173 (1984).
[26] R. E. Somekh, Journal of Vacuum Science & Technology A: Vacuum, Surfaces, and Films **2**, 1285 (1984).
[27] E. Cattan, Journal of Vacuum Science & Technology A: Vacuum, Surfaces, and Films **11**, 2808 (1993).
[28] P. M. Leufke, A. K. Mishra, A. Beck, D. Wang, C. Kübel, R. Kruk, and H. Hahn, Thin Solid Films, 1–7 (2012).
[29] D. Depla and W. Leroy, Thin Solid Films, (2012).
[30] P. Juan, H. Chou, and J. Lee, Microelectronics Reliability **45**, 1003–1006 (2005).
[31] D. Bowen, *High resolution X-ray diffractometry and topography* (Taylor & Francis, 1998).
[32] K. Kakegawa, J. Mohri, T. Takahashi, H. Yamamura, and S. Shirasaki, Solid State Communications **24**, 769–772 (1977).
[33] F. Mitsugi, Y. Yamagata, T. Ikegami, K. Ebihara, J. Narayan, and A. M. Grishin, Japanese Journal of Applied Physics **39**, 5418–5420 (2000).
[34] J. Lee and S. Desu, Ferroelectrics Letters Section **20**, 27–34 (1995).
[35] W. Wu, K. H. Wong, and C. L. Choy, Applied Physics Letters **85**, 5013 (2004).

All article content, except where otherwise noted, is licensed under a Creative Commons Attribution 3.0 Unported license. See: http://creativecommons.org/licenses/by/3.0/
Downloaded to IP: 129.13.72.198 On: Tue, 29 Apr 2014 13:56:31

[36] S. Aggarwal, A. M. Dhote, R. Ramesh, W. L. Warren, G. E. Pike, D. Dimos, M. V. Raymond, B. A. Tuttle, and J. T. Evans, Applied Physics Letters **69**, 2540 (1996).
[37] G. E. Pike, W. L. Warren, D. Dimos, B. A. Tuttle, R. Ramesh, J. Lee, V. G. Keramidas, and J. T. Evans, Applied Physics Letters **66**, 484 (1995).
[38] T. Friessnegg, S. Aggarwal, R. Ramesh, B. Nielsen, E. H. Poindexter, and D. J. Keeble, Applied Physics Letters **77**, 127 (2000).
[39] J. Lee, R. Ramesh, V. G. Keramidas, W. L. Warren, G. E. Pike, and J. T. Evans, Applied Physics Letters **66**, 1337 (1995).
[40] V. C. Lo, Journal of Applied Physics **92**, 6778 (2002).
[41] V. Bornand, S. Trolier-McKinstry, K. Takemura, and C. A. Randall, Journal of Applied Physics **87**, 3965 (2000).
[42] K. Rabe, M. Dawber, C. Lichtensteiger, C. Ahn, and J. Triscone, Physics of Ferroelectrics **30**, 1–30 (2007).
[43] J. F. Scott, C. A. Araujo, B. M. Melnick, L. D. McMillan, and R. Zuleeg, Journal of Applied Physics **70**, 382 (1991).
[44] J. F. Scott, L. Kammerdiner, M. Parris, S. Traynor, V. Ottenbacher, A. Shawabkeh, and W. F. Oliver, Journal of Applied Physics **64**, 787 (1988).
[45] S. Aggarwal, S. Madhukar, B. Nagaraj, I. G. Jenkins, R. Ramesh, L. Boyer, and J. T. Evans, Applied Physics Letters **75**, 716 (1999).
[46] S. Ray, M. Algueró, J. Ricote, M. Calzada, C. Prieto, A. de Andrés, and M. Garcia-Hernández, Materials Letters **60**, 1714–1718 (2006).

All article content, except where otherwise noted, is licensed under a Creative Commons Attribution 3.0 Unported license. See: http://creativecommons.org/licenses/by/3.0/
Downloaded to IP: 129.13.72.198 On: Tue, 29 Apr 2014 13:56:31